Large-eddy simulation of starting buoyant jets

Large-Eddy Simulation of Starting Buoyant Jets

Ruo-Qian Wang, Singapore-MIT Alliance for Research and Technology Center, Singapore; and Department of Civil and Environmental Engineering, Massachusetts Institute of Technology, USA E-mail: rqwang@mit.edu

Adrian Wing-Keung Law, School of Civil and Environmental Engineering, Nanyang Technological University, Singapore. E-mail: cwklaw@ntu.edu.sg

E. Eric Adams, Department of Civil and Environmental Engineering, Massachusetts Institute of Technology, USA. E-mail: eeadams@mit.edu

Oliver B. Fringer, Environmental Fluid Mechanics Laboratory, Stanford University, USA. E-mail: fringer@stanford.edu

Abstract

A series of Large Eddy Simulations (LES) are performed to investigate the penetration of starting buoyant jets. The LES code is first validated by comparing simulation results with existing experimental data for both steady and starting pure jets and lazy plumes. The centerline decay and the growth rate of the velocity and concentration fields for steady jets and plumes, as well as the simulated transient penetration rate of a starting pure jet and a starting lazy plume, are found to compare well with the experiments. After validation, the LES code is used to study the penetration of starting buoyant jets with three different Reynolds numbers from 2000 to 3000, and with a wide range of buoyancy fluxes from pure jets to lazy plumes. The penetration rate is found to increase with an increasing buoyancy flux. It is also observed that, in the initial Period of Flow Development, the two penetrative mechanisms driven by the initial buoyancy and momentum fluxes are uncoupled; therefore the total penetration rate can be resolved as the linear addition of these two effects. A fitting equation is proposed to predict the penetration rate by combining the two independent mechanisms.

Keywords:

Large Eddy Simulation (LES), starting phenomenon, buoyant jet, penetration

1. Introduction

Buoyant jets (or forced plumes[1]) are discharges of a volume of fluid having a density that differs from the surrounding ambient. They are widely observed in natural phenomena, such as volcanic eruptions and hydrothermal vents, and in engineering applications, such as jet propulsion and the discharge of waste water to a receiving aquatic environment. The density of a buoyant jet can be less than or greater than the ambient density, and the direction of initial momentum can be in any direction relative to the force of buoyancy. In this study we examine the behavior of starting buoyant jets in which the direction of buoyancy is aligned with the direction of initial momentum, i.e., either jets discharging a heavier fluid vertically downward or a lighter fluid vertically upward. We refer to either as "positively buoyant jets" or simply "buoyant jets".

The primary characteristics of the buoyant jet can be defined by the following parameters (Fischer et al.[2]):

$$Q_0 = \frac{1}{4}\pi D^2 U_0, \quad M_0 = \frac{1}{4}\pi D^2 U_0^2, \quad B_0 = \frac{1}{4}\pi g \frac{\Delta\rho_0}{\rho_0} D^2 U_0 \qquad (1)$$

where Q_0, M_0, and B_0 are initial volume flux, kinematic momentum flux, and kinematic buoyancy flux, respectively; g' is reduced gravity ($g\,\Delta\rho_o/\rho_o$). With these parameters, the Richardson number, R_0, which represents the ratio of buoyancy flux to initial momentum flux can also be defined as follow:

$$R_0 = \frac{l_Q}{l_M} = \frac{Q_0 B_0^{1/2}}{M_0^{5/4}} = \left(\frac{\pi}{4}\right)^{\frac{1}{4}} \left(\frac{g'D}{U_0^{\,2}}\right)^{1/2} \qquad (2)$$

We adopt the naming convention whereby the range of the buoyant jet extends from a pure jet ($R_o = 0$), through a forced plume ($0 < R_o < 0.27$), a pure plume ($R_o = 0.27$), a lazy plume ($R_o > 0.27$), and a thermal ($R_o = \infty$). Most buoyant jet studies in the literature have focused on

steady state behavior[2,3,4]. However, many buoyant jet applications are inherently short-term (e.g., the marine disposal of sediments from dredging or land reclamation), and even continuous discharges begin as starting jets or plumes. Hence, it is important to study and better understand the initial formation phase of buoyant jets.

When a buoyant jet is discharged from an orifice, a starting vortex forms immediately due to the rollup of the source fluid against the stationary ambient. This starting vortex grows until it reaches a maximum circulation state and then detaches from the trailing stem, a phenomenon commonly referred to as "pinch off"[5]. Thereafter, the starting vortex ceases to grow and is eventually engulfed by the regenerated head vortex leading the trailing stem. The analysis of the continuous process has been discussed by Law *et al.*[6]. The initial period before the engulfment is referred to as the Period of Flow Development (PFD), while the subsequent period is referred to as the Period of Developed Flow (PDF). The naming is to differentiate the two periods of development, whereby in the PFD the behavior is significantly affected by the source conditions whereas in the PDF the behavior bears similarity and can be analyzed by means of the gross discharge characteristics.

As implied above, a starting buoyant jet has two asymptotic states: (a) a starting pure jet with no buoyancy flux (R_o = 0) and (b) a thermal or starting lazy plume with negligible initial momentum flux (large R_o). The starting pure jet is a configuration of critical importance for many engineering applications (in combustion for example) and has been studied by a number of investigators. Generally, the jet is found to penetrate linearly with time in the PFD[7,8], and with the square root of time in the downstream self-similar phase[9,10,11,12] of the PDF. The other extreme of a starting lazy plume has been studied by Lundgren et al.[13], Alahyari and Longmire[14], and Pottebaum and Gharib[15]. The first two studies focused on the scaling comparison between laboratory results and the phenomenon of microburst, and showed that an appropriate scaling can significantly simplify the analysis. Pottebaum and Gharib[15] demonstrated quantitatively that the leading vortex has indeed achieved a maximum circulation. In addition, Bond and Johari[16] studied the effects of the nozzle geometry and found that the penetration rate can be divided into two periods: initial acceleration and thermal-like phases (i.e. analogous to PFD and PDF respectively). The penetration is proportional to the 1.4 power of time for the former, and the 0.5 power for the latter.

Diez *et al.*[17] used video techniques to study the characteristics of starting buoyant jets over a wide range of source buoyancy. Within the self-preserving phase, the plume was found to penetrate following the relationship of the 3/4 power of time, which was first reported by Turner[18]. Ai *et al.*[19] performed experiments on a round starting buoyant jet using Particle Image Velocimetry (PIV) and Planar Laser Induced Fluorescence (PLIF), and covered a wide range of initial density differences from Boussinesq (relative density difference $\Delta\rho_0/\rho_0 <$ 15%) to non-Boussinesq ($\Delta\rho_0/\rho_0 >$ 15%) conditions. A simplified model of the vortex-stem dynamics during the PDF was also proposed. This was followed by the subsequent analysis of Law *et al.*[6] that further addressed the dynamics of the head vortex-stem connection. Together the two works provide an overview of the physics behind the intrusion of a starting round buoyant jet and the associated penetration rate. At the same time, they concluded that the complexities of the source condition as well as the details of the transition from jet-like to plume-like behavior within the two periods need to be further investigated.

The above previous studies primarily used experimental tools to improve the understanding of the starting buoyant jet phenomenon. By contrast, numerical simulations of starting buoyant jets are less common. Iglesias *et al.*[20] and Satti and Agrawal[21,22] simulated helium jets injected into quiescent ambient air, motivated by the objective to improve the ignition of diesel engines. Satti and Agrawal[22] showed that the penetration rate was strongly dependent on buoyancy; they further investigated the effect of buoyancy on developing buoyant jets, focusing on the details of the vortex ring evolution. Despite their pioneering effort, their study did not cover enough scenarios to allow a systematic analysis of the role of the buoyancy flux in the starting phenomenon.

The present study examines the transient behavior of a starting buoyant jet in the initial period of PFD using the Large-Eddy Simulation (LES) approach; the study is part of a larger effort which includes numerical, experimental and field observations to investigate the near-source transport of sediment released in coastal waters. In particular, we aim to quantify the effect of buoyancy on the penetration rate based on the simulation results. LES provides a versatile approach for turbulence modeling that resides at an intermediate level between the Reynolds Average Navier-Stokes (RANS) and the Direct Numerical Simulation (DNS) approaches. The algorithm used in this study is the Dynamic Mixed Model (DMM) which is

employed in a Navier-Stokes solver developed at the Environmental Fluid Mechanics Laboratory at Stanford University.

In Section 2, the LES model used in this study is briefly described. This is followed in Section 3 by a validation effort for buoyant jets, in which we use the LES model to simulate steady pure jets and lazy plumes, whose limiting behaviors are well understood (e.g. Fischer et al.[2]; Wang and Law[23]). It will be shown that the present LES model can simulate the main features of these flows including the decay in the centerline velocity and concentrations, as well as the velocity and concentration widths. Following the validation, we perform a set of numerical experiments over a range of starting buoyant jets in Section 4. Section 5 provides the summary and conclusions.

2. LES Approach

2.1 Governing Equations

The governing equations for the LES approach are the spatially-filtered continuity, Navier-Stokes and scalar transport equations with the Boussinesq approximation as follows:

$$\frac{\partial \overline{u}_i}{\partial x_i} = 0, \tag{3}$$

$$\frac{\partial \overline{u}_i}{\partial t} + \frac{\partial \overline{F}_{ij}}{\partial x_j} = \overline{S}_i, \tag{4}$$

$$\frac{\partial \overline{T}}{\partial t} + \frac{\partial \overline{R}_j}{\partial x_j} = 0, \tag{5}$$

where

$$\overline{F}_{ij} = \overline{u}_i \overline{u}_j + \overline{p}\delta_{ij} - \upsilon \frac{\partial \overline{u}_i}{\partial x_j} + \tau_{ij}, \tag{6}$$

$$\overline{S}_i = -g\beta(\overline{T} - T_0)\delta_{i3} \tag{7}$$

$$\overline{R}_j = \overline{u}_j \overline{T} - \kappa \frac{\partial \overline{T}}{\partial x_j} + \chi_j, \tag{8}$$

where the over-bar represents a spatially-filtered quantity. u_i (i=1,2,3) are the Cartesian velocity components in the direction of x_i. Other quantities are as follows: t is time, p is pressure, g is the gravitational acceleration, T is a scalar (e.g., density or temperature), T_0 is the background scalar, $\beta = \frac{1}{T_0}\frac{\partial \rho}{\partial T}$ is the coefficient of thermal expansion, υ is the kinematic viscosity, and κ is the scalar diffusivity. Note that all the equations are subjected to the Einstein rule of summation.

The subfilter-scale terms τ_{ij} and χ_j are specified as:

$$\tau_{ij} = \overline{u_i u_j} - \bar{u}_i \bar{u}_j \tag{9}$$

$$\chi_j = \overline{u_j T} - \bar{u}_j \bar{T} \tag{10}$$

These two terms are modeled with the dynamic mixed subgrid-scale model, details of which can be found in Zang et al.[24].

2.2 Numerical Methods

The governing equations are transformed to generalized curvilinear coordinates and discretized with a finite-volume formulation on a non-staggered grid[25]. The discretization includes: 1) a semi-implicit scheme with Crank-Nicholson for the diagonal viscous and diffusive terms and Adams-Bashforth for the other terms; 2) accurate upwind-difference schemes on the convective terms; and 3) second-order accurate central differences on all the other spatial differential terms. The convective terms of the momentum equations (Eq. 4) are discretized using the QUICK scheme, whereas the convective terms for the scalar transport equation (Eq. 5) are discretized using the SHARP scheme to avoid spurious oscillations[26,27].

The numerical code has previously been validated by a series of comparisons with standard experiments. A 3D lid-driven cavity flow was reproduced by Zang et al.[24] as the first validation of this model. Subsequently, LES was performed on a range of round jets in cross flows with low and moderate Reynolds numbers[28,29]. The trajectory and entrainment

characteristics were shown to agree with the experiments very well. In addition, upwelling flows were simulated by Zang and Street[30] and Cui and Street[31], and the turbulent current beneath nonlinear free-surface waves[32] and the flow over a wavy boundary[33] were also convincingly reproduced by the present code. Recently, Zedler and Street[34] and Chou and Fringer[35] further developed the code to incorporate bed-load sediment transport. In summary, the LES algorithm of Zang et al.[24,25] has been demonstrated to be a practical and efficient LES scheme that is suitable for a range of turbulent flows. In the present study we extend the validation to include jets and plumes discharging into quiescent environments. The parallel version of the code that we used here was developed by Cui and Street[31].

2.3 Flow configuration

The computational domain used in this study is a rectangular volume with a square horizontal cross-section that extends to 1.2 m × 1.2 m× 1.5 m for validation, and 0.5 m × 0.5 m × 1.5 m for the remaining production runs in the Cartesian coordinates of x, y and z respectively as shown in Figure 1(a). Note that the domain size is reduced for the prediction runs so as to control the computational expense and the production results of penetration rate is free of impact (which will be proved later). At t=0, a buoyant jet with positive buoyancy (i.e. the buoyancy force is along the jet direction) is issued at a uniform velocity U_0 into a homogeneous and stationary ambient fluid with density ρ_0. The relative density difference between the jet flow and the ambient is $\Delta\rho_0 / \rho_0$. The buoyant jet is discharged at the top of the domain through a circular nozzle which has a diameter D=5 cm. Thus, the size of the domain can also be expressed as $24D \times 24D \times 30D$ and $6D \times 6D \times 30D$ for validation and production respectively, which shall limit the domain of investigation of the penetrative behavior. The computational domain is discretized into a stretched mesh with increased refinement along the vertical axis (see Figure 1(b)).

The boundary conditions are also presented in Figure 1(a). The velocity field is specified at the top boundary as an incoming uniform jet with a velocity field given by $w((x-3D)^2+(y-3D)^2<D^2/4,\ z=0)=U_0$, while the other boundaries are all outflow boundaries. Following the recommendation of Yuan[36], the outflow boundary condition is essentially the "no gradient" condition, which has limited effect on the starting results before the flow structure penetrates

beyond the domain. A constant volume flux, determined from the prescribed inflow velocity U_0, is enforced at the inlet.

3. Validation

In this section, the LES model is validated specifically for the study of buoyant jets discharging to quiescent environments by comparing the simulation results to experiments for the asymptotic cases of a pure jet and a lazy plume, the behaviors of which have been well studied[2,19,23]. Two types of validations are performed: (a) steady state and (b) starting phenomenon. In addition to the validation, the numerical simulations serve to optimize the required grid spacing.

It is necessary to pinpoint the tip of the penetrative front in order to determine the penetration rate of a starting buoyant jet. We search for the tip at a particular time by scanning the concentration field layer by layer from the bottom towards the top of the computational domain. The first vertical position at which the threshold concentration was exceeded was determined to be the tip front. We chose a threshold concentration equal to 10% of the initial concentration, i.e. 10% of $\Delta\rho_o / \rho_0$, but because the front is characterized by steep scalar gradients, its location is quite distinct and not very sensitive to small variations of the chosen threshold concentration. An example of the concentration field is shown in Figure 2.

3.1 Jet

For a pure jet, the controlling characteristic is the initial momentum flux. Strictly speaking, a pure jet does not possess any density difference with the ambient, i.e. $\Delta\rho_o / \rho_0 = 0$. However, in order to visualize the scalar structure, the jet density is increased slightly to $\Delta\rho_0 / \rho_0 = 10^{-99}$ in the validation simulations so that the density can act as a tracer to illustrate the scalar distribution but without introducing significant buoyancy. The initial velocity of the jet, U_0, is 0.05 m/s. The corresponding Reynolds number is $Re=U_0D/\nu=2500$, i.e. the jet is turbulent at the source.

3.1.1 Steady state

Since the present simulation using the LES approach is transient, an averaging period which is large enough to average the instantaneous variations of the flow is required to show the steady state characteristics of the mean velocity and concentration fields. For this reason, the mean characteristics of the flow averaged over different periods with a sampling frequency of 1 Hz are drawn in Figure 3 for the pure jet case (and later in Figure 6 for the lazy plume case).

The velocity and concentration decay rates along the center line of the pure jet are compared with the experimental results from Wang and Law[23] in Figure 3(a). From the figure, the axial velocity and concentration retain their initial values within a potential core of about 6*D*. Downstream in the Zone of Established Flow (ZEF), the axial velocity and concentration decay continuously with a rate that decreases with penetration distance. It can be observed that the agreement with the experimental results is good with a sampling duration of 40s covering 60-100s. From Figure 3(a), more scatter can be noted for the concentration decay, but the agreement remains satisfactory. The equivalent axial velocity and concentration radius of the jet are shown in Figure 3(b). To evaluate the jet expansion, the boundary is defined by the locations within a particular horizontal plane where the axial velocity (or concentration) is 37% (1/e) of its maximum value. The growth of the velocity width (b_w) and the concentration width (b_c) defined in this manner indicates, respectively, the spreading rate of the axial velocity and concentration spreading in the vertical direction. Simulations indicate that both widths increase with penetration distance, in a manner consistent with experiments in the ZEF (i.e. $z/D>6$). Note that a consistent radius is observed in the potential core region.

3.1.2 Starting pure jet

The penetration rate of a starting pure jet represented by the temporal rate of change of the vertical position of the tip is shown for different grid sizes in Figure 4(a). From the figure, the penetration rate with 64×64×384 grid cells is similar to the simulation with 80×80×480 grid cells, thus implying that the simulation with 64×64×384 grid cells has sufficient grid

resolution. To demonstrate the absence of boundary effects, penetration rates in different domain sizes are compared in Figure 4(b). The penetration rates overlap each other, which indicates that in the early stage of development, the penetration rate is not impacted by the domain size. Therefore, the small domain size of 0.3m*0.3m*1.5m is used for the production results.

The dimensionless penetration rate, i.e. the slope of η versus the square root of time, is shown in Figure 5, where $\eta = z_t /(M_0)^{1/4} = z_t /(\frac{\pi}{4} D^2 U_0^2)^{1/4}$ and z_t is the position of the front. As discussed before, the initial period of varying penetration rate can be referred to as the Period of Flow Development by Ai et al.[19]. After the flow is developed with self-similar profiles, the penetration rate possesses a constant power law relationship with time, and the slope on a log-log scale would become nearly a constant. From the simulation results, the slope of the last section for the simulation results is found to be equal to 4.0, which matches almost exactly the result of Ai et al.[8]. Hereto, the simulations successfully reproduce the penetration of a starting pure jet.

3.2 Plume

Following the pure jet validation above, a further study is conducted for the validation of a lazy plume whose characteristics are controlled by the initial buoyancy flux B_0. For these simulations, the initial velocity U_o is taken to be a small value of 0.05 m/s, while the density difference is set to be $\Delta\rho_0 / \rho_0 = 7 \times 10^{-2}$. The corresponding Richardson number R_o is 3.49 which lies within the lazy plume regime[1].

3.2.1 Steady state

Figs. 6(a) and 6(b) show that, using an averaging period duration of 40 s and a sampling frequency of 1 Hz, the axial velocity and concentration decay along the centerline become consistent beyond t=40 s. The results agree the experimental measurements by Wang and Law[23] beyond z=6D. One interesting aspect of the lazy plume is that the axial velocity

increases very quickly in the laminar region near the source before transition into turbulence following the decay in the self-similar region. The concentration decay is also well predicted with virtual origin correction, which assumes that a point source at z=2.5D can properly represents the nozzle of a lazy plume[37]. Note that the initial concentration remains constant in the laminar region until the velocity peaks. For the growth rate, Figure 6 shows that the velocity and concentration (virtual origin corrected) spreading also agree with the proposed values by Wang and Law[23], despite the equivalent radius narrows slightly in the potential core. Summarizing the steady state results in Sections 3.1.1 and 3.2.1, it appears that the centerline flow characteristics approach steady state earlier than the spreading width characteristics. This is somewhat expected, since axial flow development near the centerline of a jet or plume is dominant while the lateral development depends on the transverse turbulent shear dispersion and thus a larger time scale.

Besides the mean flow characteristics, comparisons were also made between simulated turbulence characteristics and experimental data reported by Wang and Law[23]. The simulated longitudinal turbulence intensities along the centerline, $\sqrt{\overline{w_c'^2}}/w_c$ for both a non-buoyant jet and a pure plume were about 25% less than the corresponding experimental values of 0.26 and 0.27, while the simulated results for $\sqrt{\overline{u_c'^2}}/w_c$ were about 10% below the experimental values of 0.19 for both cases. The simulated transverse profiles of $\overline{w'u'}/\overline{w_c}^2$ were similar to the experiments in both magnitude and shape, but showed somewhat more variability.

3.2.2 Starting lazy plume

A numerical study on the dependence of grid size is first conducted. The results, presented in Figure 7, suggest that a grid mesh finer than 64×64×384 is required for the penetration analysis. According to Figure 8 the non-dimensional penetration rate has a time power of 0.78 in the PDF, which is very close to the results of 3/4 in Diez et al.[17] and Ai et al.[19]. This comparison between the numerical and experimental studies validates the code for the simulations of the starting lazy plume. According to these validations and balancing the computational expense, the grid mesh of 64×64×384 is used for the following simulations.

In summary, the present LES model performs credibly for the asymptotic cases of a pure jet and a lazy plume. Its transient performance is particularly convincing when the simulation results are compared with previous experimental data. The steady state results are also reliable, and can be further improved if longer simulations are performed.

4. Buoyant jet

4.1 Penetration rate with starting buoyant jets

The penetration rates of buoyant jets with different initial buoyant fluxes (hence, different values of R_0) are shown in Figure 9. Initially all jet fronts penetrate at the same rate until tU_0/D=0.8. Afterwards, the pure jet penetrates linearly with time, whereas jets with higher buoyancy penetrate faster. When the jets reach the self-similar phases (e.g. tU_0/D=3.5-4 for a buoyant jet with R_0=2.95), the penetration rates of the buoyant jets approach an asymptotic value as described above, i.e. 3/4 of the square root of time.

According to the results, the development of the penetration rate can be divided into three phases: the initial overlapped phases, the accelerated phase, and finally the asymptotic phase. To isolate the effects of buoyancy flux, the penetration distance by the pure jet is subtracted from the total penetration distance, and the excess penetration distances z_B are shown versus time in Figure 10. For comparison, the excess penetration distances of jets with different initial momentum fluxes (i.e. Reynolds numbers) are shown in the same figure.

The three phases of penetration rate can be interpreted by the relationship of the two driving mechanisms, i.e. the initial momentum flux and the buoyancy inducement. In the initial overlapped phase, buoyancy does not have time to significantly accelerate the penetration. Therefore, the momentum flux dominates the driving force and the penetration distances overlap each other. During the accelerated phase, the potential energy contained in the buoyancy flux is transformed by gravitational acceleration to kinetic energy. Thus, the penetration rate differs for different buoyancy fluxes as shown in Figures 9 and 10. Figure 10 isolates the buoyancy effect from the initial momentum in terms of excess penetration

distance: for the same density difference but different initial momentum, penetration distances are found to overlap each other. This suggests that the total penetration distance can be resolved as the sum of the separate effects of initial momentum and buoyancy. Because these two factors are uncoupled, the relationship between them appears to be linear.

At the final self-similar phase (or PDF), the total penetration rate decreases due to the greater entrainment of ambient fluid. At the same time, the momentum flux and buoyancy inducement interact nonlinearly with each other, resulting in the front advancing with an asymptotic limit of $t^{3/4}$.

4.2 Penetration equation

A key objective of the present study is to examine the time-dependent penetration of buoyant jets in the PFD. As discussed in the introduction, the penetration in the PFD is more complex than in the PDF due to a lack of self similarity. The source conditions, in particular, significantly affect the penetration behavior in PFD. These conditions include the velocity profile and history at the source, nozzle geometry, laminarity, and the presence of overpressure. The LES results obtained in the study are relevant for the penetration of a round turbulent jet with a piston-driven type uniform velocity profile without overpressure. The following shows how a proper choice of scaling can yield a general fitting equation for the penetration rate within the PFD.

First, we explore non-dimensionally the analysis of the excess penetration, z_B. Generally, for a turbulent flow we expect that $z_B = \phi(t, B_o, Q_o, M_o)$. However, since z_B is the penetration distance beyond that of a pure jet, M_o may be insignificant, and B_o and Q_o can be used as repeating variables to yield normalizing time, penetration distance and momentum scales:

$$t' = \frac{Q_0^{4/5}}{B_0^{3/5}} \qquad z' = \frac{Q_0^{3/5}}{B_0^{1/5}} \qquad M_o' = Q_o^{4/5} B_o^{2/5} \tag{10}$$

Noting that $M_o/M_o' = R_o^{-4/5}$, Figure 11(a) plots z_B/z' versus t/t' for various R_o. For $R_o < 1.2$ (solid lines), a reasonable fit is provided by

$$\ln(z_B / z') = 2\ln(t / t') - 2.3 \tag{11}$$

which results in

$$z_B / D = 0.10 \frac{B_0}{Q_0 D} t^2 \quad or \; z_B = 0.10 g' t^2 \tag{12}$$

For free-falling objects in a gravitational field without significant resistance, the proportionality coefficient in Eq. 12 would be 0.5. The present coefficient of ~0.1 is substantially less. This implies that strong resistance, probably in the form of a drag force and momentum sharing by entrained ambient stationary fluid, is acting on the starting vortex by the ambient fluid. The fact that R_o = 1.2 is well on the lazy plume side of a pure plume, suggests that for most buoyant jets, z_B is indeed independent of M_o as hypothesized.

An alternative relationship covering the full range of Richardson numbers used in our model simulations ($0 < R_0 < 3$) is provided by normalizing penetration by a different scale; thus

$$t'' = t' = \frac{Q_0^{4/5}}{B_0^{3/5}} \text{ and } z'' = \frac{Q_0^{1/5} M_0^{1/2}}{B_0^{2/5}}, \tag{13}$$

Figure 11(b) plots non-dimensional penetration versus time using Equation 13, from which

$$\ln(z_B / z'') = 2.4\ln(t / t'') - 3, \tag{14}$$

or

$$z_B = 0.05 \frac{M_0^{0.5} B_0^{1.04}}{Q_0^{1.72}} t^{2.4} \tag{15}$$

Because it has a stronger physical basis and is valid for most buoyant jets, Equation (12) is used to predict the following total penetration distance.

Second, the penetration distance driven by the initial momentum flux (i.e., the penetration of a pure jet) can be determined from Figure 9 as

$$z_M = 0.53 U_o t \tag{16}$$

or

$$z_M / D = 0.47 \frac{M_0^{3/2}}{Q_0^2} t, \tag{17}$$

where, as expected from physical arguments, z_M is proportional to $U_0 t$. The coefficient of 0.53 reflects the roll-up of the discharged fluid to form the starting vortex. It is close to the theoretical value of 0.50 expected in the potential core region of a non-buoyant jet if, following arguments of Prandtl[38], we assume that the stagnation pressure is the same on either side of the front. Summing up the penetration due to momentum and buoyancy, the total penetration distance can be expressed as

$$z_t / D = z_B / D + z_M / D = 0.10 \frac{B_0}{Q_0 D} t^2 + 0.47 \frac{M_0^{3/2}}{Q_0^2} t \tag{18}$$

Again this equation is applicable only in the PFD region when the penetration is led by the starting vortex. After the pinch-off and when the jet stem engulfs the starting vortex and regenerates a leading vortex, the penetrative behavior would evolve into the PDF behavior described in Ai *et al.*[19].

4.3 Penetration measured by different flow parameters

For buoyant jets, the flow characteristics can be represented by a number of parameters including the scalar concentration and the spatial components of velocity and vorticity. While the results in the previous sections are established based on the concentration front, it is pertinent to examine whether the penetration is similar for the other parameters. For this purpose, we consider a buoyant jet having a uniform initial velocity U_0 = 0.05 m/s, and initial relative density difference $\Delta\rho_0 / \rho_0 = 4 \times 10^{-4}$. The threshold tests described in Section 3 are then repeated by replacing the value of concentration with the values of velocity and vorticity

components, i.e. u, v, w and ω_x, ω_y, ω_z. The penetration distances extracted from these different fields are shown in Figure 12, which shows that the penetration rates are almost identical, although the concentration field penetrates slightly faster than the velocity field. This suggests that there is no significant discrepancy between the various fields regarding the penetration analysis. In other words, the intrusion can be taken as a shock front in the PFD.

5. Summary and Conclusions

A numerical study using the LES approach has been conducted to investigate the penetration behavior of a starting buoyant jet during the PFD. The behavior of the two asymptotic cases of a pure jet and a lazy plume are first reproduced to validate the numerical code. The steady-state results of the centerline decay and the growth rate of concentration and velocity fields compare favorably with the experimental data reported in the literature. The corresponding transient simulations are also consistent with the experiments reported previously. These validations show that the present numerical model is effective and sufficiently accurate for the analysis.

After the validation, the model is used to simulate starting turbulent buoyant jets with three different Reynolds numbers from 2000 to 3000, and a wide range of buoyancy effects from pure jets to lazy plumes. The penetration front generally advances faster with higher buoyancy. More importantly, the penetrative distances induced by the initial buoyancy fluxes and by the initial momentum fluxes are found to be independent; therefore, the total penetration distance can be treated as a linear combination of these two parts. An equation is proposed to approximate the penetration behavior of a starting buoyant jet in the PFD by performing curve fitting to the numerical results. Future experiments would be desirable to verify the present conclusions.

Acknowledgments

This work was supported, in part, through the CENSAM IRG, Singapore-MIT Alliance for Research and Technology. The authors wish to acknowledge Rex Britter for useful theoretical discussions, and Yi-ju Chou for help in parallel computing and code implementation.

References

[1] Morton, B.R. (1959). Forced plumes. *Journal of Fluid Mechanics*, 5, 151-163.

[2] Fischer, H.B., List, E.J., Koh, R.C.Y., Imberger, J., Brooks, N.H. (1979). *Mixing in inland and coastal waters*, New York: Academic Press.

[3] List, E.J. (1982). Turbulent jets and plumes. *Annual Review of Fluid Mechanics*, 14, 189-212.

[4] Lee, J.H., Chu, V. (2003). *Turbulent Jets and Plumes: A Lagrangian Approach* 1st ed., Springer.

[5] Gharib, M., Rambod, E., Shariff, K. (1998). A universal time scale for vortex ring formation. *Journal of Fluid Mechanics*, 360, 121-140.

[6] Law, A.W.K., Ai, J.J., Yu, S.C.M. (2007) Leading vortex of a starting forced buoyant plume. *Proc., 9th Asian Symposium on Visulization*, 4-6 June, Hong Kong, China.

[7] Cossali, G., Coghe, A., Araneo, L. (2001). Near-field entrainment in an impulsively started turbulent gas jet. *AIAA Journal*, 39(6), 1113-1135.

[8] Ai, J.J., Yu, S.C.M., Law, A.W.K., Chua, L.P. (2005). Vortex dynamics in starting square water jets. *Physics of Fluids*, 17(1), 014106-014118.

[9] Johari, H., Zhang, Q., Rose, M., Bourque, S.M. (1997). Impulsively started turbulent jets. *AIAA Journal*, 35(4), 657-662.

[10] Hill, P.G., Ouellette, P. (1999). Transient turbulent gaseous fuel jets for diesel engines. *Journal of Fluids Engineering, Transactions of the ASME*, 121(1), 93-101.

[11] Joshi, A., Schreiber, W. (2006). An experimental examination of an impulsively started incompressible turbulent jet. *Experiments in Fluids*, 40(1), 156-160.

[12] Bajpai, S., Tirumkudulu, M. (2008). An experimental study of impulsively started turbulent axisymmetric jets. *European Physical Journal B*, 61(3), 293-297.

[13] Lundgren, T., Yao, J., Mansour, N. (1992). Microburst modelling and scaling. *Journal of Fluid Mechanics*, 239, 461-488.

[14] Alahyari, A., Longmire, E. (1995). Dynamics of experimentally simulated microbursts. *AIAA Journal*, 33(11), 2128-2164.

[15] Pottebaum, T. & Gharib, M. (2004). The pinch-off process in a starting buoyant plume. *Experiments in Fluids*, 37(1), 87-94.

[16] Bond, D., Johari, H. (2005). Effects of initial geometry on the development of thermals. *Experiments in Fluids*, 39(3), 589-599.

[17] Diez, F. J., Sangras, R., Faeth, G.M., Kwon, O.C. (2003). Self-preserving properties of unsteady round buoyant turbulent plumes and thermals in still fluids. *Transactions of the ASME. Journal of Heat Transfer*, 125(5), 821-851.

[18] Turner, J. S. (1962). The 'Starting Plume' in neutral surroundings. *Journal of Fluid Mechanics*, 2, 583-594

[19] Ai, J.J., Law, A.W.K., Yu, S.C.M. (2006). On Boussinesq and non-Boussinesq starting forced plumes. , *J. Fluid Mechanics*, 558, 357-386.

[20] Iglesias, I., Vera, M., Sánchez, A.L., Liñán, A. (2005). Simulations of starting gas jets at low Mach numbers. *Physics of Fluids*, 17(3), 38105-38109.

[21] Satti, R.P., Agrawal, A.K. (2006). Computational analysis of gravitational effects in low-density gas jets, *AIAA Journal*, 44(7), 1505-1515.

[22] Satti, R.P., Agrawal, A.K. (2008). Computational study of buoyancy effects in a laminar starting jet. *International Journal of Heat and Fluid Flow*, 29(2), 527-539.

[23] Wang, H., Law, A.W.K. (2002). Second-Order Integral Model for a Round Turbulent Buoyant Jet. *Journal of Fluid Mechanics*, 459, 397-428.

[24] Zang, Y., Street, R.L., Koseff, J.R. (1993). Dynamic mixed subgrid-scale model and its application to turbulent recirculating flows. *Physics of Fluids A Fluid Dynamics*, 5(12), 3186-3196.

[25] Zang, Y., Street, R., Koseff, J. (1994). A non-staggered grid, fractional step method for time-dependent incompressible Navier-Stokes equations in curvilinear coordinates. *Journal of Computational Physics*, 114(1), 18-33.

[26] Leonard, B. (1979). A stable and accurate convective modeling procedure based on quadratic upstream interpolation, *Comp. Meth. Appl. Mech. Eng.,* 19, 59–98.

[27] Zang, Y. (1993), *On the Development of Tools for the Simulation of Geophysical Flows*, PhD thesis, Stanford University, Stanford, CA

[28] Yuan, L.L., Street, R.L. (1998). Trajectory and entrainment of a round jet in crossflow. *Physics of Fluids*, 10(9), 2323-2335.

[29] Yuan, L., Street, R., Ferziger, J. (1999). Large-eddy simulations of a round jet in crossflow. *Journal of Fluid Mechanics*, 379, 71-104.

[30] Zang, Y., Street, R. (1995). Numerical simulation of coastal upwelling and interfacial instability of a rotating and stratified fluid. *Journal of Fluid Mechanics*, 305, 47-75.

[31] Cui, A., Street, R.L. (2004). Large-Eddy Simulation of Coastal Upwelling Flow. *Environmental Fluid Mechanics*, 4(2), 197-223.

[32] Hodges, B., Street, R. (1999). On simulation of turbulent nonlinear free-surface flows. *Journal of Computational Physics*, 151(2), 425-482.

[33] Calhoun, R., Street, R.L., (2002). Patterns on a free surface caused by underwater topography: A laboratory-scale study. *International Journal of Remote Sensing*, 23(8), 1609-1620.

[34] Zedler, E.A., Street, R.L. (2006). Sediment transport over ripples in oscillatory flow. *Journal of Hydraulic Engineering*, 132(2), 180-193.

[35] Chou, Y., Fringer, O.B. (2008). Modeling dilute sediment suspension using large-eddy simulation with a dynamic mixed model. *Physics of Fluids*, 20(11), 115103-13.

[36] Yuan, L.L. (1997), *Large Eddy Simulations of a Jet in Crossflow*, PhD thesis, Department of Mechanical Engineering, Stanford University, Stanford, CA.

[37] Hunt, G.R., Kaye, N.G. (2001). Virtual origin correction for lazy turbulent plumes. *J. Fluid Mechanics*, 435:377-396.

[38] Prandlt, L (1952). Essentials of fluid dynamics. New York: Hafner Publishing Co.

List of Figures

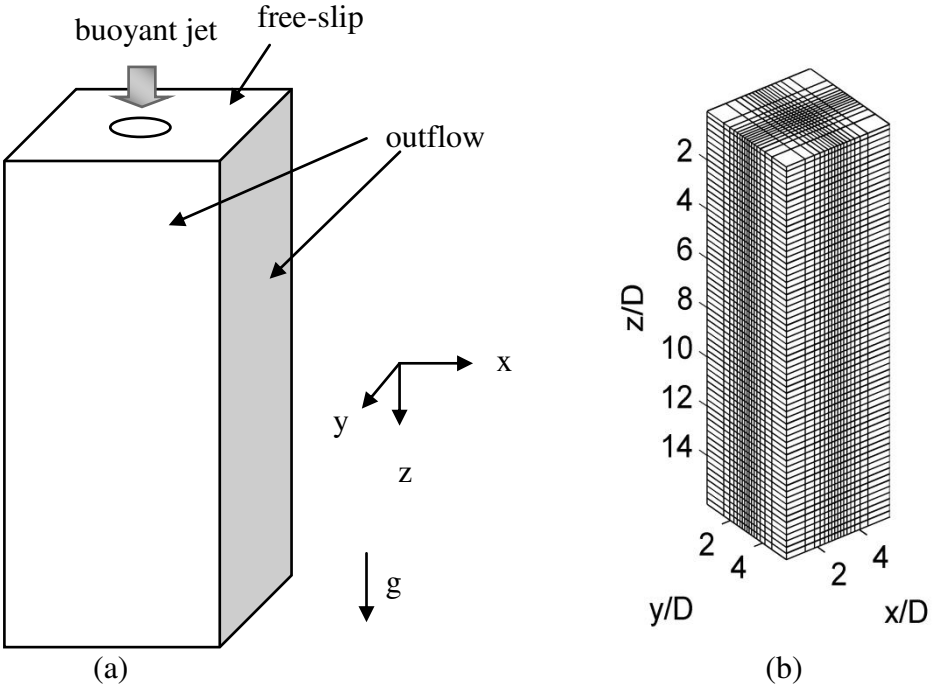

Figure 1 Computational domain: (a) boundary conditions (not to scale); (b) a typical grid mesh (only every 4th mesh point shown in each direction; the center of the jet outlet is at x=3D, y=3D, Z=0)

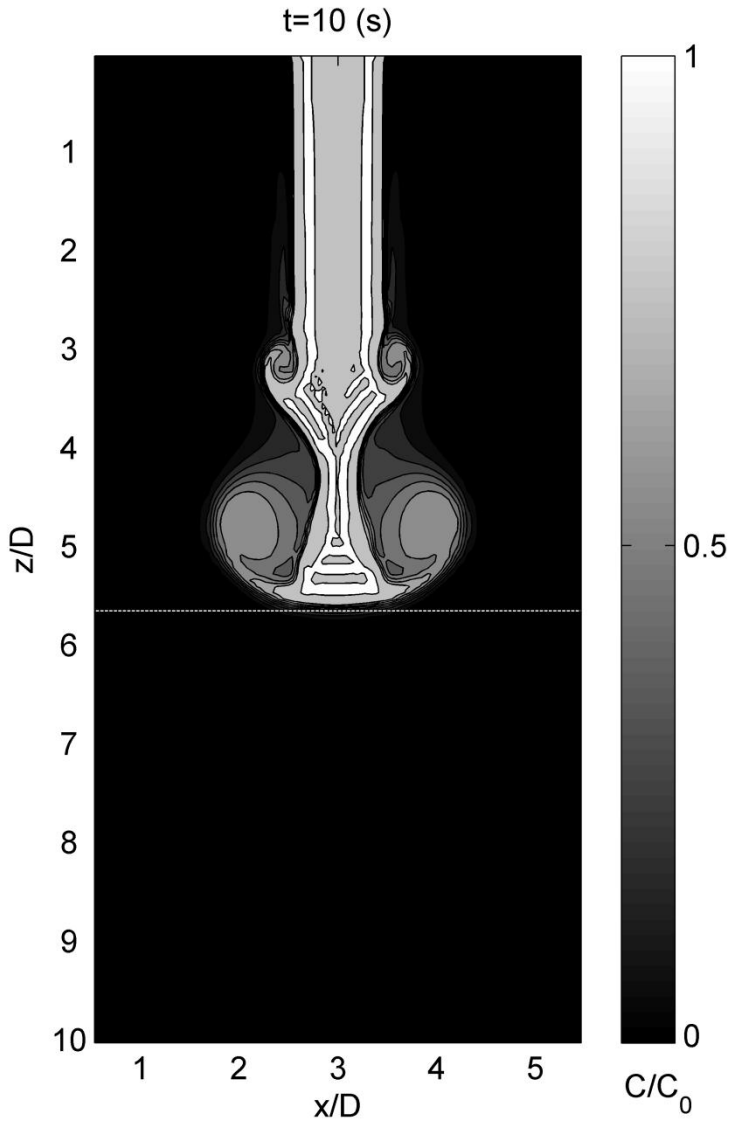

Figure 2 Penetrative front of the buoyant jet (Re=2500, R_0=0.186). The dash line denotes the location of the jet front.

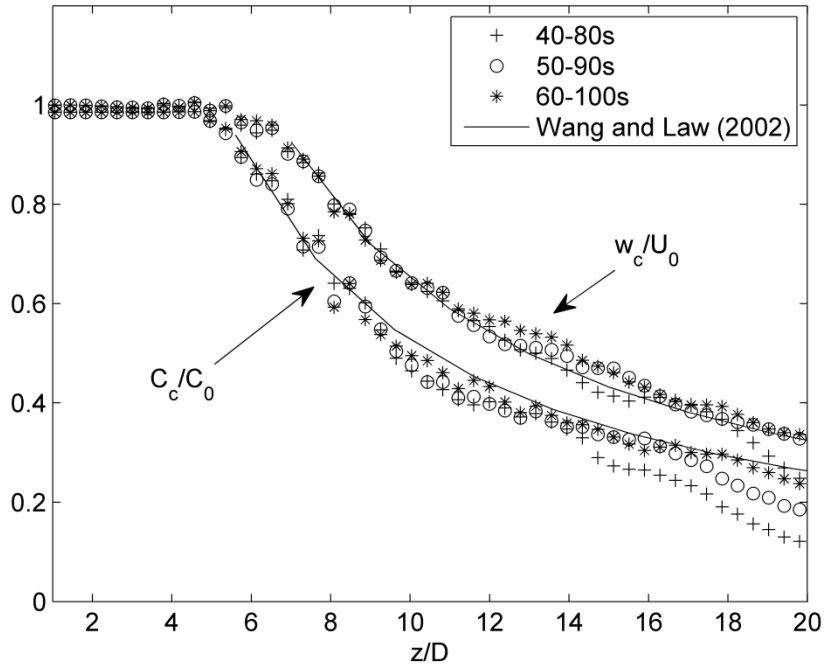

(a)

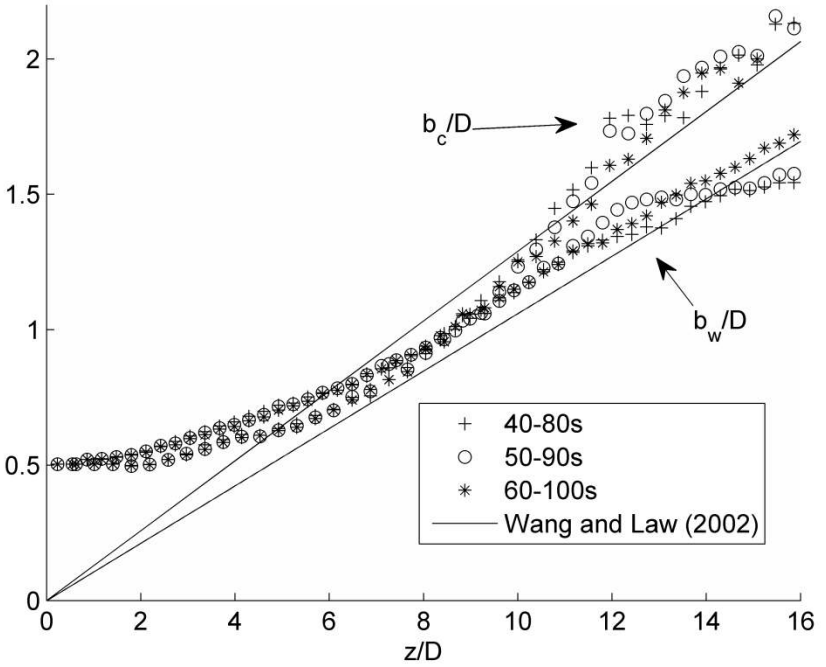

(b)

Figure 3 (a) Decay of the mean axial velocity and concentration of a pure jet with different averaging periods; (b) Growth of the mean velocity and concentration width of a pure jet with different averaging periods.

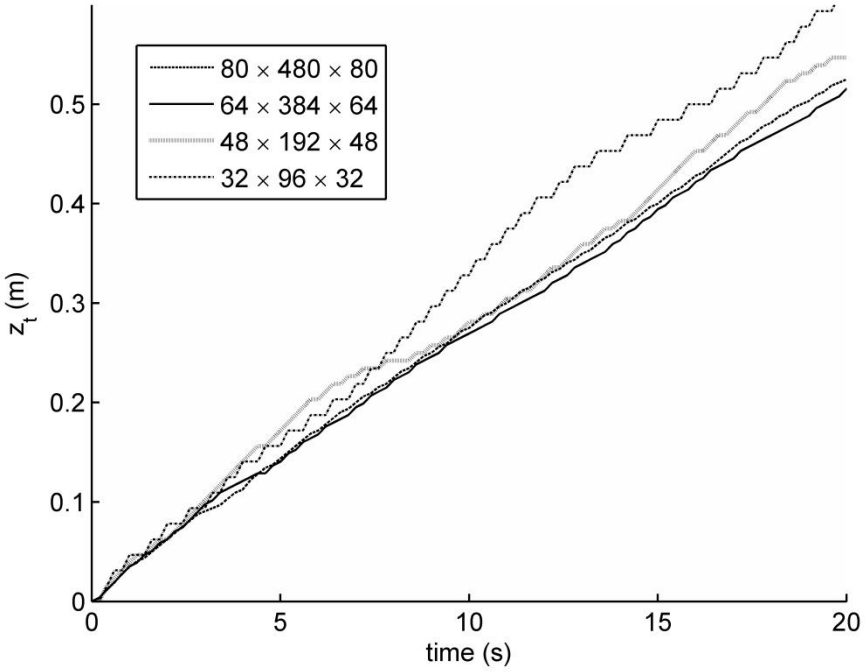

(a)

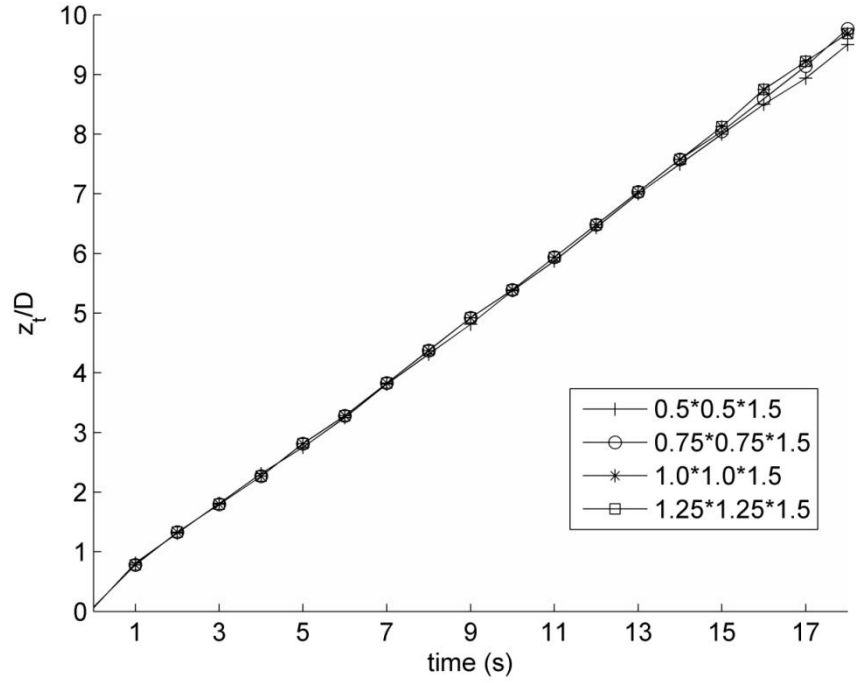

(b)

Figure 4 Penetration rate of a pure jet with different grid sizes (domain size length unit in m).

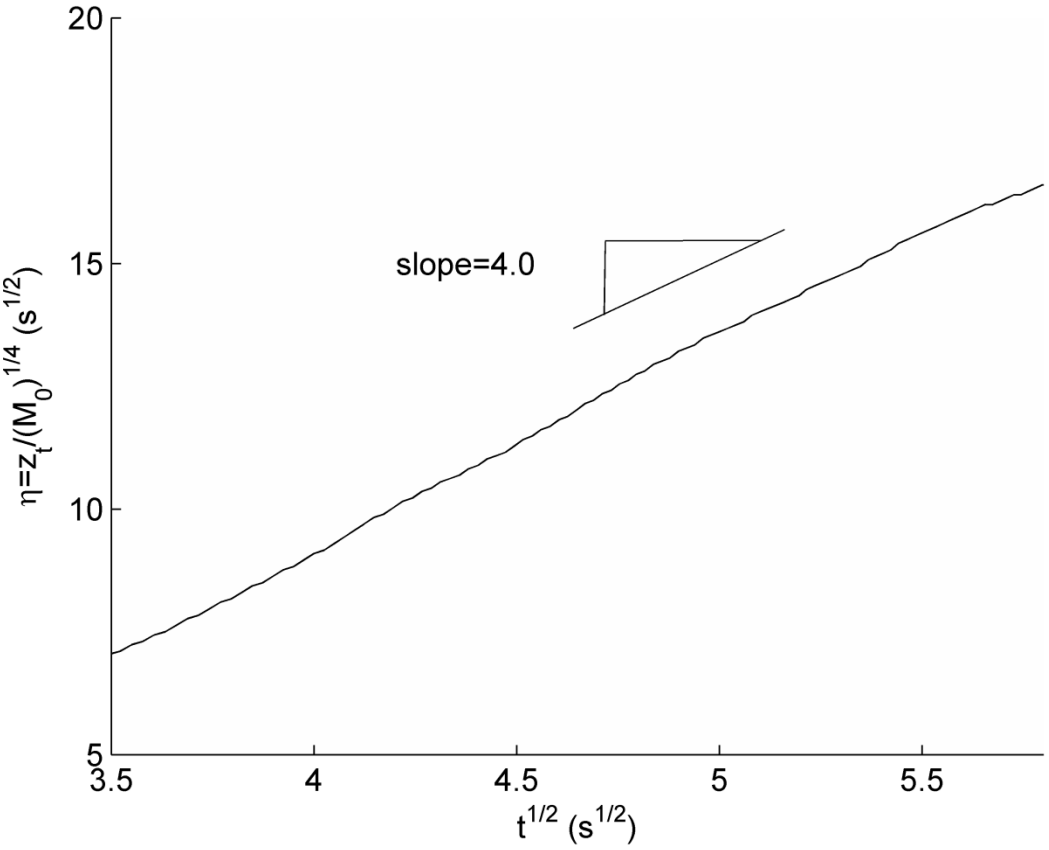

Figure 5 Dimensionless penetration rate of a pure jet

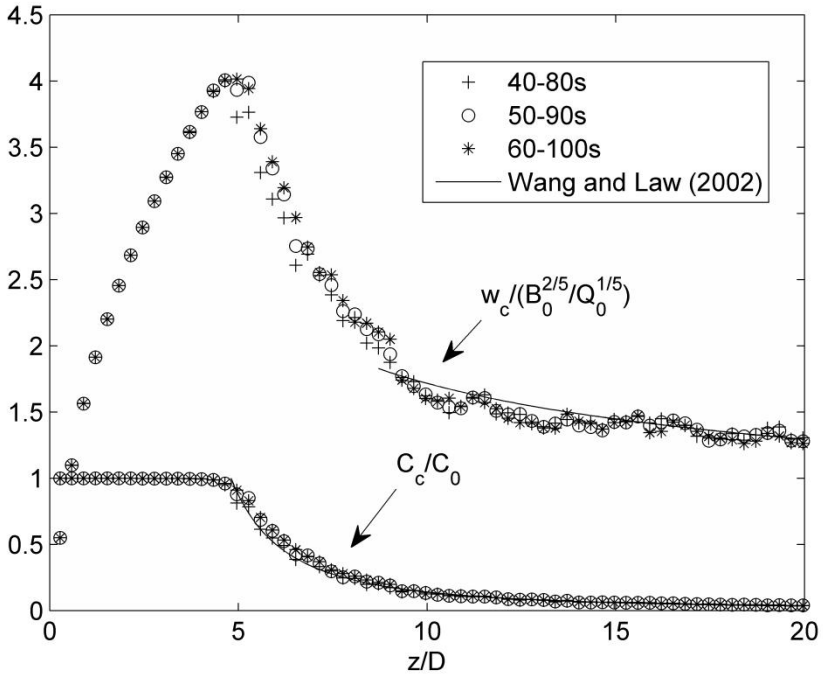

(a)

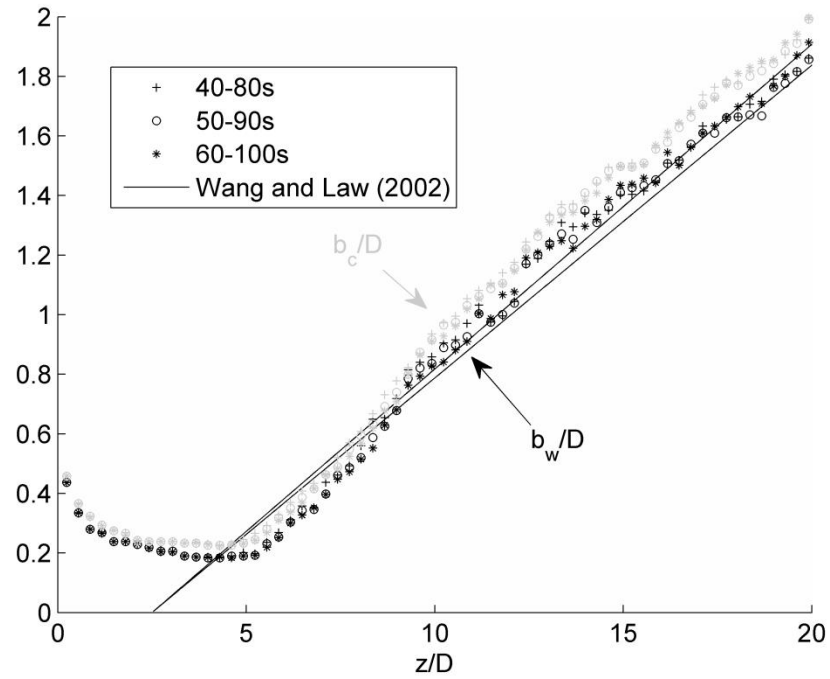

(b)

Figure 6 Validation for lazy plume: (a) Decay of the mean axial velocity and concentration of a lazy plume and (b) growth of the mean velocity and concentration width of a lazy plume with different averaging periods

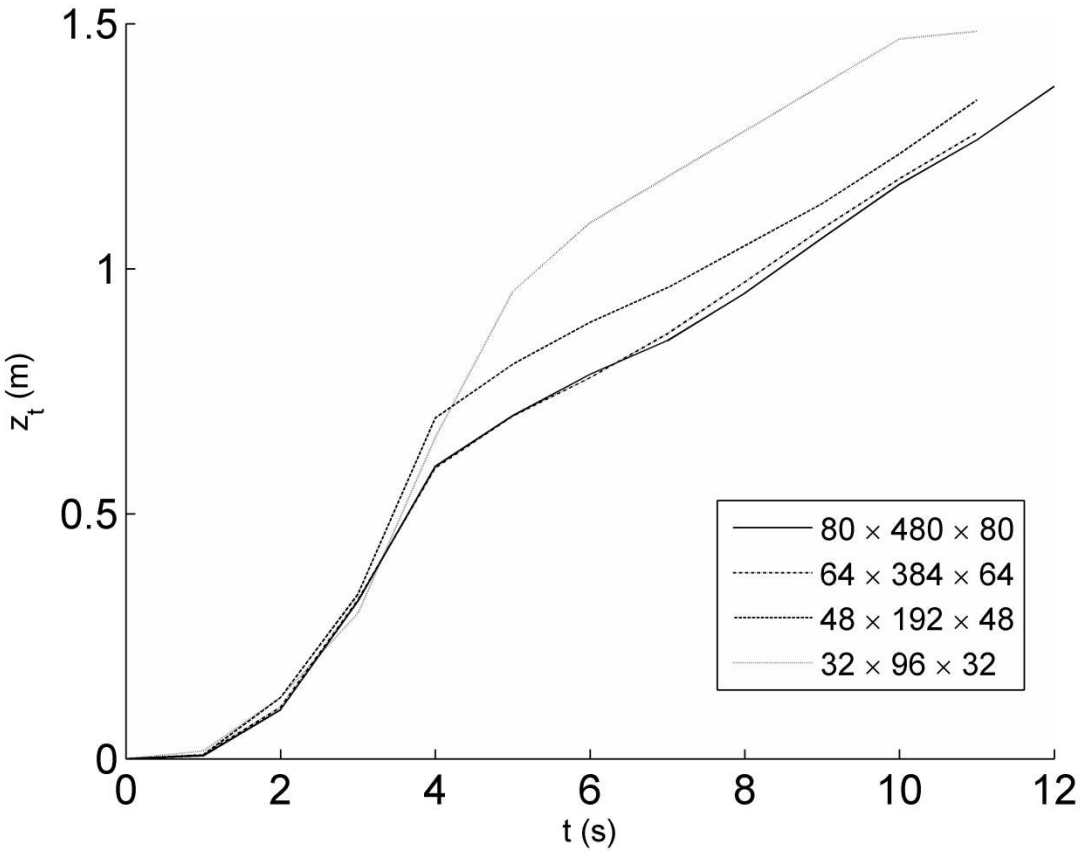

Figure 7 Penetration rate of a lazy plume with different grid sizes

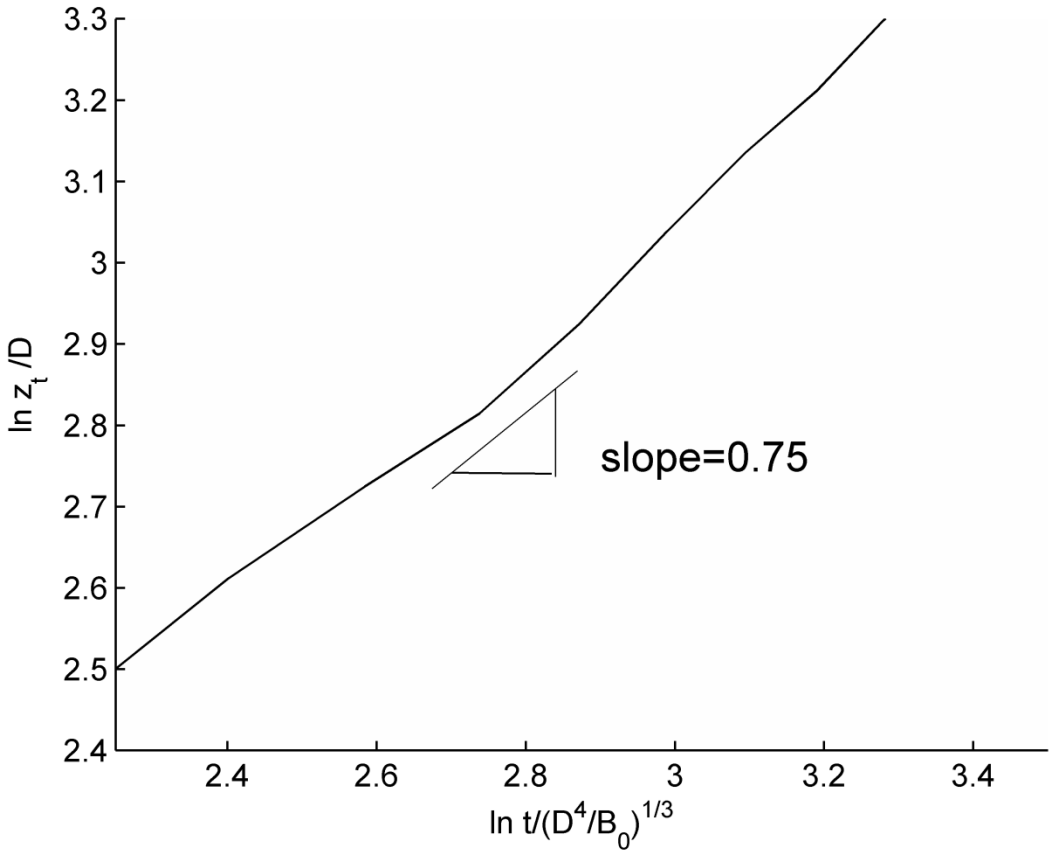

Figure 8 Dimensionless penetration rate of a lazy plume

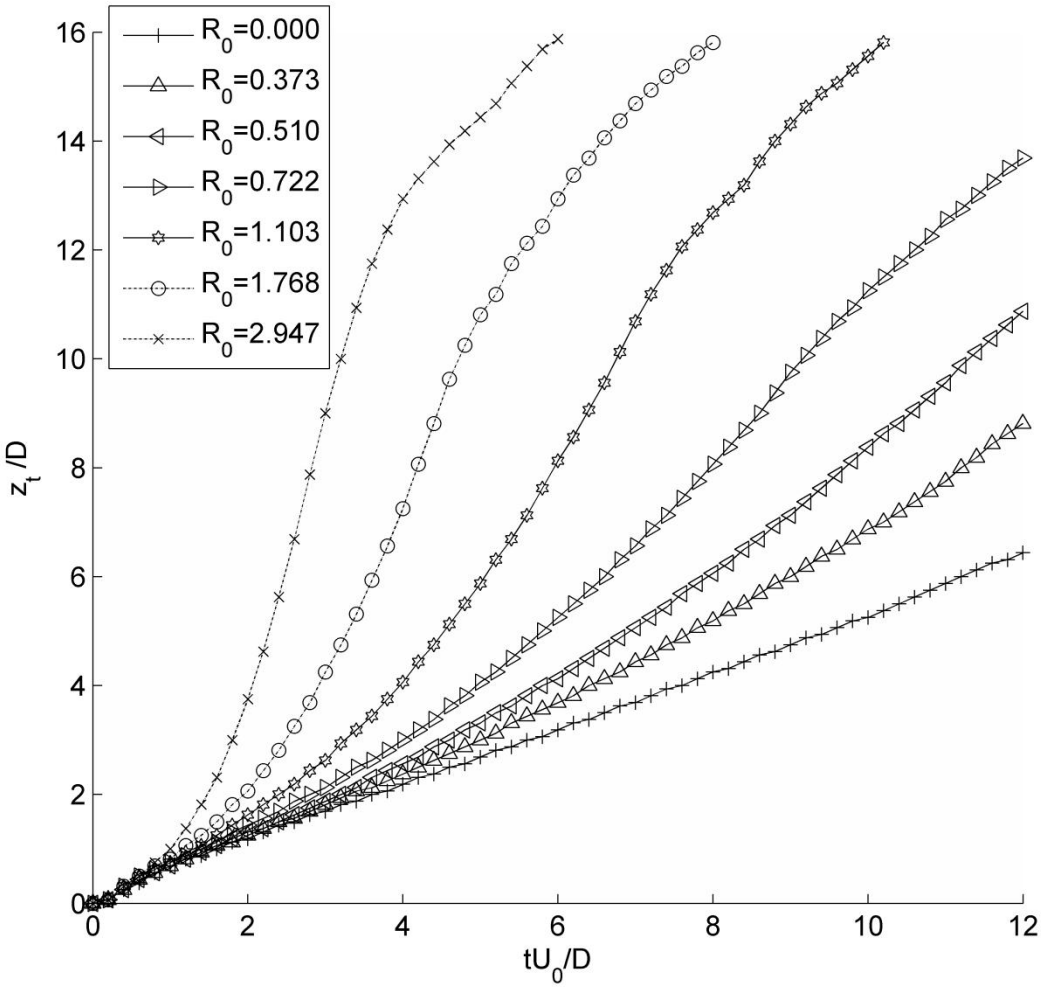

Figure 9 Penetration of buoyant jets in the PFD under different buoyancy fluxes

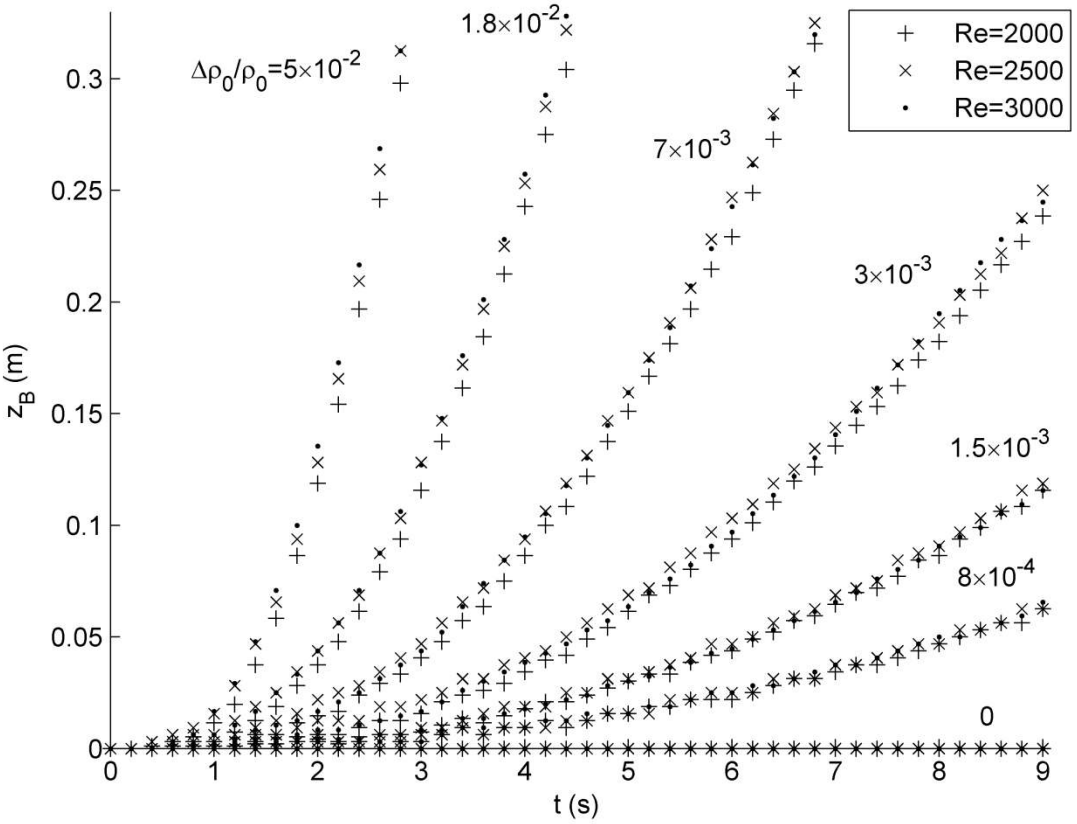

Figure 10 Excessive penetration induced by various buoyancy fluxes

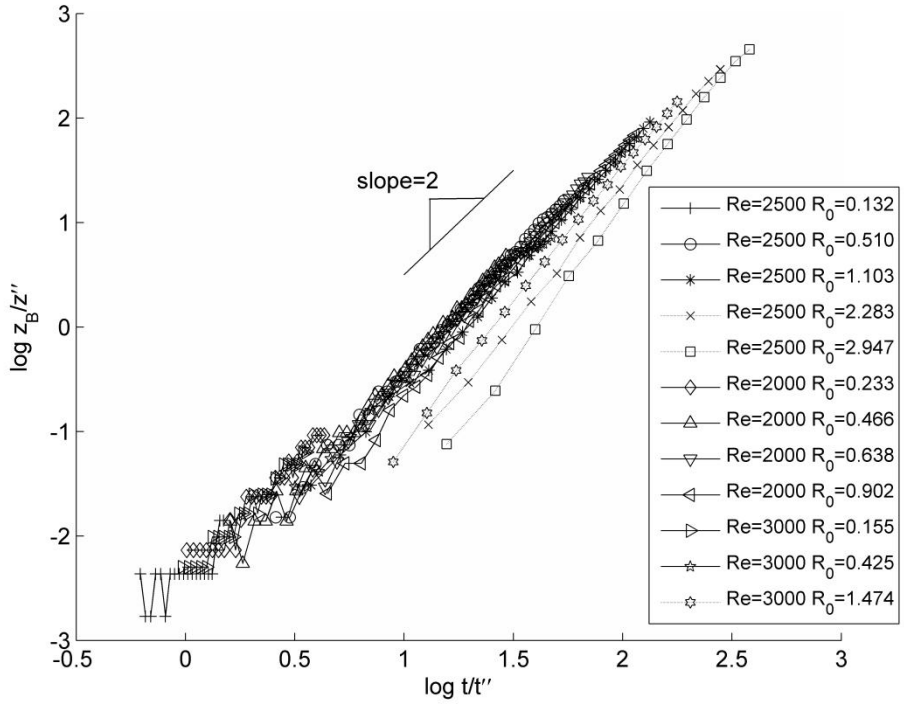

(a)

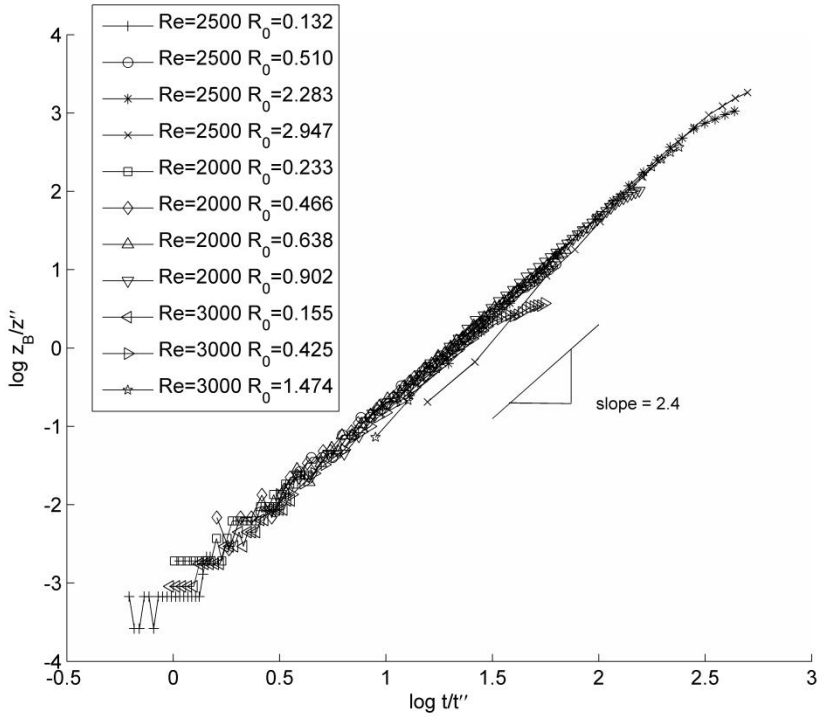

(b)

Figure 11 Dimensionless excess penetration of buoyant jets induced by buoyancy fluxes with dimensionless time

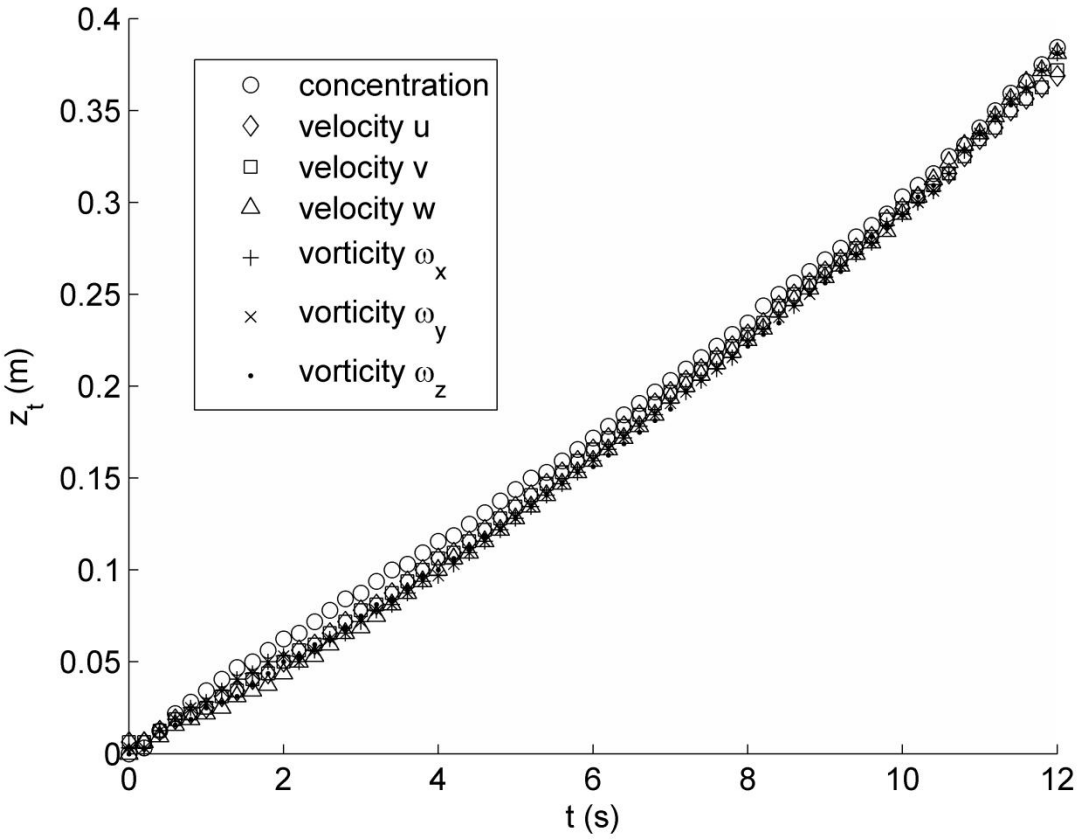

Figure 12 Penetration distance with different flow characteristics